the particles localize to fixed positions (Fig. 3, C to F). This cannot be observed in the one-dimensional case. Two-dimensional calculations for the large-particle case are not depicted, but they also confirm the morphology shown in one dimension by Fig. 1A. Additionally, crystallization effects are seen in the two-dimensional calculation, just as in the small-particle case. We note, however, that the detailed crystal arrangement may change in three dimensions.

The method introduced here allows us to capture the synergistic interactions that occur in self-assembling mixtures of flexible copolymers and hard particles. It reveals how enthalpic and entropic effects in multiphase media contribute to the observed morphologies and, as in our case, can lead to entropically driven particle crystallization. The versatility of this theory allows us to study the role of copolymer architecture, particle shape, and composite composition, all without making a priori assumptions about the structure of the system. Furthermore, we can compare the free energies of competing structures and construct equilibrium phase diagrams. Overall, the technique can offer valuable assistance in exploring the rich variety of mesostructures that can occur in polymer-particle mixtures and in designing hybrid materials with the desired morphology.

References and Notes

1. M. Templin *et al.*, *Science* **278**, 1795 (1997).
2. D. Zhao *et al.*, *Science* **279**, 548 (1998).
3. S. Stupp, P. V. Braun, *Science* **277**, 1242 (1997).
4. M. W. Matsen, F. S. Bates, *Macromolecules* **29**, 1091 (1996) and references therein.
5. P. Tarazona, *Mol. Phys.* **52**, 81 (1984).
6. G. J. Vroege, H. N. W. Lekkerkerker, *Rep. Prog. Phys.* **55**, 1241 (1992) and references therein.
7. The "free energy" discussed here is actually a dimensionless free energy density: $F \rightarrow NF/\rho_0 k_B TV$, where k_B is the Boltzmann constant and T is absolute temperature.
8. The Tarazona DFT was selected because it is a simple and physical approach specifically developed to reproduce the liquid-solid transition in hard spheres. Some DFTs more accurately describe the liquid equation of state but fail to predict the liquid-solid transition; other approaches are more computationally intensive.
9. N. F. Carnahan, K. E. Starling, *J. Chem. Phys.* **51**, 635 (1969).
10. F. Drolet, G. H. Fredrickson, *Phys. Rev. Lett.* **83**, 4317 (1999).
11. This approach may also be better suited to examining morphologies that lose their symmetry on the scale of the particle size. See the "crystallization" effect in Fig. 3 as an example.
12. Y. Bohbot-Raviv, Z.-G. Wang, *Phys. Rev. Lett.* **85**, 3428 (2000).
13. V. Lauter-Pasyuk *et al.*, *Physica B* **241**, 1092 (1997).
14. V. Lauter-Pasyuk *et al.*, *Physica B* **248**, 243 (1998).
15. B. Hamdoun *et al.*, *J. Phys. (France) II* **6**, 493 (1996).
16. J. Huh, V. V. Ginzburg, A. C. Balazs, *Macromolecules* **33**, 8085 (2000).
17. The volume fraction has been increased from 0.15 to 0.20 so as to better illustrate "crystallization" effects. Aside from such effects, the morphology is found to be the same as at 0.15.

18. Supported by the U.S. Department of Energy, NSF, the Army Research Office, and the Engineering and Physical Sciences Research Council (UK).

12 March 2001; accepted 24 May 2001

REPORTS

Diapiric Flow at Subduction Zones: A Recipe for Rapid Transport

Paul S. Hall* and Chris Kincaid

Recent geochemical studies of uranium-thorium series disequilibrium in rocks from subduction zones require magmas to be transported through the mantle from just above the subducting slab to the surface in as little as ~30,000 years. We present a series of laboratory experiments that investigate the characteristic time scales and flow patterns of the diapiric upwelling model of subduction zone magmatism. Results indicate that the interaction between buoyantly upwelling diapirs and subduction-induced flow in the mantle creates a network of low-density, low-viscosity conduits through which buoyant flow is rapid, yielding transport times commensurate with those indicated by uranium-thorium studies.

Volcanism associated with the subduction of oceanic lithosphere is the primary source of new continental crust and contributes to the chemical differentiation of the crust-mantle system. The mechanism of melt generation at subduction zones and transport to the surface remains uncertain. Proposed models include diapiric flow of a hydrous and/or molten component (*1–5*), porous flow of magma (*6*), and melt propagation through fractures (*7, 8*). Constraints on the melting process at subduction zones come from both geochemical (*2, 3, 9–13*) and geophysical (*14, 15*) studies. In particular, excesses of ^{238}U relative to ^{230}Th observed in rocks from the Mariana (*13*) and Tonga-Kermadec (*11*) arcs require the time between the fractionation event responsible for the disequilibrium (i.e., slab dehydration) and eruption of the magma to be as short as ~30 thousand years (ky). Here we report the results of a series of laboratory experiments conducted to evaluate the characteristic time scales and morphologies of the diapiric flow model.

Conceptual models of mantle diapirism at subduction zones (*1–5*) invoke the growth of gravitational instabilities within a thin buoyant layer at the upper surface of the subducting slab to explain arc volcanism (Fig. 1A). Individual instabilities detach from the layer and rise through the mantle wedge as diapirs along trajectories determined by the balance between buoyancy forces and drag from subduction-induced motion in the mantle wedge. The diapir model can explain some geophysical observations of magmatism at subduction zones, including the observed regularity of spacing between discrete volcanic centers along arcs (d = 70 km) and the presence and character of secondary, or transverse, volcanism at many arcs (*1, 16, 17*). It also accounts for many of the petrologic characteristics of arc rocks (*3, 4*). Previous laboratory studies of the diapir model were concerned with the physics of instability growth from a line of buoyant, low-viscosity fluid embedded within a stagnant, viscous fluid and focused on spatial variations in the resulting flow (*1, 17, 18*). Our work extends these earlier experiments by including the effect of flow in the viscous fluid and focusing on temporal variations in the patterns of buoyant flow.

Results are presented from a series of 10 laboratory experiments in which we simulated subduction-driven (matrix) flow with a concentrated sucrose solution and flow of buoyant (hydrated or partially molten) mantle with a dyed alcohol solution (Fig. 1B). The buoyant fluid is introduced from a point source, representing what would be a single site of instability growth from a linear buoyancy source [the distribution of instabilities along a linear buoyancy source was previously investigated and yielded a regular spacing of ~70 km between instabilities (*1*)]. This parameterization of the buoyancy source is necessary in investigating the temporal evolution of the flow because of the experimental difficulties inherent in maintaining a constant linear source of compositionally buoyant fluid. The flux of buoyant fluid and the velocity of the subducting plate are varied to investigate a range in the relative strength of buoyant and forced flow. Laboratory and mantle length scales are related by assuming that the depth of the buoyancy source in the lab apparatus, D (17 cm), corresponds to the uniform depth of the Wadati-Benioff zone observed directly beneath island arcs (125 km). With this fixed length scale, the Mylar velocity can be scaled to a subduction velocity in the mantle through the dimensionless ratio of buoyant flow velocity (from Stokes' law for a spherical body) to subduction velocity (U_0) given by

Graduate School of Oceanography, University of Rhode Island, Narragansett, RI 02882, USA.

*To whom correspondence should be addressed: E-mail: phall@gso.uri.edu

$$U^* = \frac{\Delta\rho g r^2}{3\mu_0 U_0} \quad (1)$$

where $\Delta\rho$ is the difference between matrix and buoyant fluid densities, g is gravitational acceleration, r is diapir radius, and μ_0 is the dynamic viscosity of the matrix. Once a velocity scale is obtained, the flux of buoyant fluid can be scaled with the dimensionless buoyancy number (*19*)

$$B_n = \frac{\Delta\rho g Q}{\mu_0 U_0^2} \quad (2)$$

where Q is the volumetric flux of buoyant fluid. In addition to providing a measure for scaling buoyancy fluxes to the mantle (Table 1), characterizing flow with B_n facilitates comparison between individual experiments. Values of B_n considered in these experiments range from 10^{-5} to 10^{-3}.

The experiments revealed three distinct flow regimes as functions of B_n based on diapir transit times and flow morphology (Fig. 2). At low values of B_n ($\sim 10^{-4}$ to 10^{-5}), the buoyant fluid forms diapirs of uniform radius (0.3 to 0.4 cm) at regular time intervals (Fig. 2A). A thin tail of buoyant fluid trails behind the diapir, which is severed from the source. Diapirs ascend at a uniform velocity, maintaining a systematic spacing along their trajectory, which is deflected from the vertical by strong matrix flow. Transit times are defined as the time elapsed from the point at which a diapir detaches from the buoyancy source until it impacts the surface and correspond directly to the times given by uranium-thorium series (U-Th) disequilibrium studies. In this regime, transit times vary between 1200 and 2400 s (~ 3 to 6×10^6 years, scaled to the mantle). These times are at the extreme limit necessary to preserve a ^{10}Be signature in erupted magmas and are too long to account for the U-Th series data.

Intermediate values of B_n ($\sim 10^{-4}$) result in diapirs forming at irregular intervals, but with a range of sizes. The larger diapirs ascend more quickly, occasionally overtaking the slower, smaller diapirs. When this occurs, a single, larger diapir is formed while some buoyant fluid is left behind, creating an enlarged trailing conduit (Fig. 2B). When an ascending diapir encounters such a conduit, it is transported rapidly along the length of the conduit. This interaction between ascending diapirs and fossil conduits has previously been documented in laboratory studies of mantle plumes (*20*). Transit times in this regime vary from 300 to 1600 s (~ 0.7 to 3×10^6 years, scaled to the mantle). These times are consistent with the preservation of a ^{10}Be signal in erupted magmas but are too long to preserve any U-Th disequilibrium.

High values of B_n ($\sim 10^{-3}$ to 10^{-4}) lead to a networked flow regime wherein several fossil conduits resulting from interaction between ascending diapirs merge to form a single continuous network spanning an appreciable portion of the working fluid (e.g., 60 to 75% of the vertical distance from the Mylar to the surface). Ascending diapirs encountering this network (Fig. 2C) are transported rapidly along its length (e.g., rates of 5 cm s^{-1}). Flow in this regime exhibits some of the characteristics of a low-amplitude solitary wave, but the nonuniform nature of the conduit makes a detailed comparison to studies

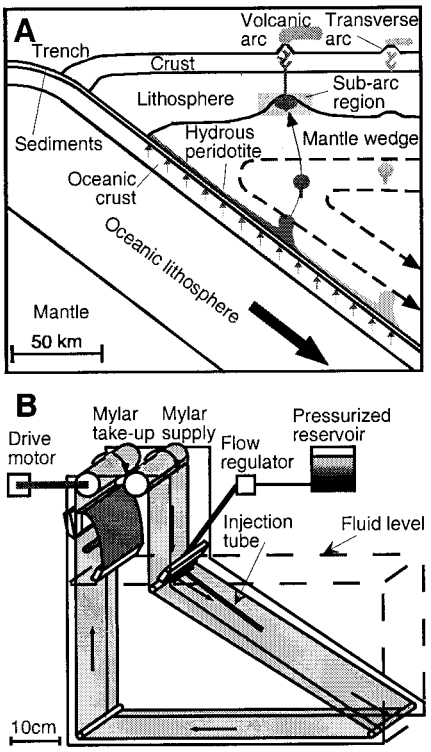

Fig. 1. Schematic diagrams of conceptual and laboratory subduction models. (**A**) Pressure-dependent dehydration reactions within the basaltic crust of a subducting oceanic plate release water into the overlying mantle wedge, creating a thin layer of hydrous peridotite above the slab that extends along the slab surface at this depth (e.g., into and out of the page) (*24*). This layer is less dense and less viscous than peridotite in the overlying mantle wedge and develops Rayleigh-Taylor instabilities (*1*). During ascent, diapirs pass from relatively warm mantle through progressively hotter mantle before finally moving through the colder mantle immediately beneath the crust. The diapir will exchange heat with the surrounding mantle through diffusion. (**B**) A diagram of the experimental apparatus showing the polycarbonate superstructure used to model subduction within a glass tank (80 cm by 40 cm by 40 cm) filled with a concentrated sucrose working fluid. Plate-driven flow is modeled by pulling Mylar sheeting through the working fluid along a fixed trajectory (subduction angle = 40°) with a synchronous high-torque motor. Buoyant fluid (a dyed alcohol solution) is introduced along the surface of the Mylar at depth from a pressurized reservoir through a small tube positioned along the surface of the Mylar. The flux is controlled by a flow regulator.

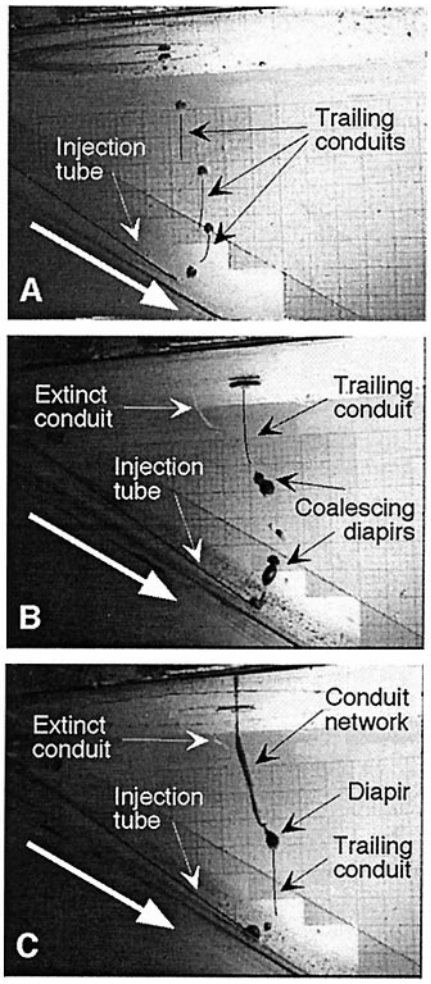

Fig. 2. Backlit images from experiments depicting three observed flow morphologies. The view is across the width of the tank, roughly parallel to the strike of the trench axis. The grid on the tank wall is 2.54 cm by 2.54 cm squares (bold lines) subdivided into 0.635 cm by 0.635 cm squares (fine lines). The direction of Mylar motion is indicated by bold white arrows. Narrow conduits of remnant low-density fluid trailing the ascending diapirs are highlighted for clarity. Plate-driven flow versus buoyant flow interaction regimes include the following: (**A**) Steady diapirism ($B_n \sim 10^{-5}$). Diapirs of nearly equal size rise along paths deflected from vertical by strong flow in the ambient fluid. There is no interaction between diapirs. (**B**) Coalescing diapirs ($B_n \sim 10^{-4}$). Diapirs of different sizes form, with some of them interacting to produce both larger diapirs and trailing conduits. An extinct conduit, which has been sheared and advected toward the trench by flow driven by the subducting plate, is visible. (**C**) Networked flow ($B_n \sim 10^{-3}$). Several coalesced diapirs and their overthickened conduits have merged to form a continuous network. A diapir is about to encounter the conduit network and be transported, in seconds, to the surface. Several extinct conduits are visible.

of solitary wave phenomena under more idealized conditions difficult (*21*). Transport times in this regime range from 4 to 400 s (e.g., 10^4 to 10^6 years), depending on the percentage of the ascent path covered by the conduit network. The rapid transport characteristic of this regime is capable of preserving the high degrees of U-Th disequilibrium observed at arcs (*11, 13*).

In the networked flow regime, the supply of buoyant fluid to the subarc region is observed to be episodic. Horizontal flow near the surface of the ambient fluid deforms and tilts over the conduit, which is then abandoned while a new portion of conduit is reestablished by subsequent diapirs. The time scale for reestablishing a networked conduit is dependent on a new sequence of diapir formation, interaction, and ascent, estimated in these experiments to average around 400 s (or 10^6 years).

Results from these laboratory experiments indicate that buoyant flow can occur in a number of different morphologies within the wedge, including the diapir (head and tail) and an interconnected conduit network. The thermal evolution of the buoyant material during ascent is controlled by a balance between lateral diffusion of heat and vertical advection (*22*). Diffusion is a function of the local temperature in the mantle wedge and the characteristic length scale of the particular flow. We use a scaling law for thermal diffusion, along with length scales measured for each of the flow morphologies observed in the experiments, to calculate diffusion time scales (Table 1). The ratio, Ω, of diffusion time scales to measured ascent times (Table 1) allows us to estimate pressure-temperature (*P-T*) trajectories for the observed flows (Fig. 3). Large diapirs move quickly relative to the rate of heat diffusion ($\Omega \geq 1$) and are therefore unlikely to experience heating sufficient to melt except on the outermost periphery. Small diapirs and thin diapir tails exchange heat efficiently with their surroundings, essentially maintaining thermal equilibrium during ascent ($\Omega \ll 1$). These flows therefore follow the local temperature gradient in the mantle (i.e., the geotherm) in *P-T* space and experience hydrous melting at depth. However, as material moves through the thermal maximum in the wedge and into progressively cooler surroundings, this trajectory leads out of the hydrous melting region, and melt will freeze out before reaching the subarc region (Fig. 1A). Networked flow ($\Omega \sim 0.2$) exhibits a damped response in *P-T* space, a behavior intermediate to these two scenarios. Material is heated enough during ascent to cross the wet peridotite solidus and experience melting but is then able to traverse the region of relatively colder mantle fast enough to avoid cooling and freezing out of melt. According to this scenario, diapirs are not the source of melt, but the vehicle for producing the conduit network, which in turn is optimal for transporting hydrated material to the subarc region.

Although the diapir model of subduction magmatism has fallen out of favor in recent years, results from these experiments reaffirm the feasibility of this model. Earlier studies demonstrated the ability of diapiric instabilities to explain a number of geophysical and petrological observations (*1, 3, 4, 16, 17*). The ability to produce interconnected

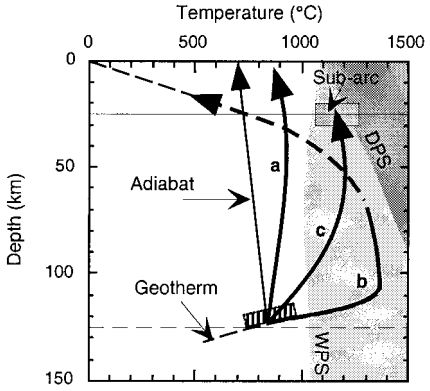

Fig. 3. Plots showing estimated *P-T* paths for buoyant material transported in the various flow morphologies from the experiments, relative to wet (*25*) (WPS) and dry (*26*) (DPS) peridotite solidii. The dashed line at 125 km marks the slab surface, and the line at 25-km depth represents the base of the lithosphere in the subarc region. Trajectories for upwelling from above the slab surface (hatched area) are estimated for different values of Ω (Table 1). Three paths are shown, in addition to an adiabatic path ($\Omega \gg 1$). Path a ($\Omega \sim 1$): This is the trajectory taken by large diapirs that ascend more rapidly than they are heated. No melting is expected. Path b ($\Omega \ll 1$): This trajectory is taken by slow moving (e.g., small diapirs) or extremely thin (e.g., diapir tails, porous flow) features and is dominated by diffusion. Initial heating and melt production (solid) are followed by cooling and freezing out of melt (dashed line) before material reaches the subarc region. Path c ($\Omega \sim 0.2$): This trajectory is taken by material ascending through networked conduits. Sufficient heating occurs during passage through the hot region of the wedge to produce wet melting, but passage through the cooler portion of the wedge is rapid enough to prevent freezing out of melt before reaching the subarc region. The geotherm is determined from a numerical model of subduction (*27*) (9 cm year^{-1} plate rate, thin overriding plate) and taken along a curved trajectory from the surface of the slab to the base of the crust. Dimensional temperatures are calculated with a mantle potential temperature of 1325°C and an adiabatic gradient of 0.5°C km^{-1}. It is interesting to note that path c trajectories may be slightly subparallel to H_2O activity contours within the subarc region. The implications of water partitioning from melt at these shallow depths warrant further study.

Table 1. Experimental and scaling parameters. The top part of the table shows buoyant flow parameters, and the bottom part shows a comparison of laboratory and scaled mantle parameter ranges.

Upwelling type	*P-T* path (Fig. 3)	r_l (cm)	r_m* (km)	t_d† (ky)	t_l (s)	t_m‡ (ky)	Ω
Diapir							
Large	a	0.75	5.5	960	293	718	1.3
Small	b	0.30	2.2	150	1350	3300	0.05
Tail	b	0.01	0.1	0.32	293	718	0.0004
Network	c	0.05	0.36	4.1	8	20	0.2
Porous flow§	b	–	10^{-6}	10^{-11}	–	714	10^{-14}

	μ_0 (Pa s)	μ/μ_0‖	$\Delta\rho$ (kg m^{-3})	U_0 (cm min^{-1})	U_0 (cm year^{-1})	Q (cm^3 min^{-1})	Q¶ (km^3 ky^{-1})
Laboratory	10^2	10^{-5}	400	1–2.5	–	0.05–0.5	–
Mantle	10^{18}	10^{-2}–10^{-4}	100	–	5–12.5	–	0.135–1.35

*Radii of flow features in the mantle, r_m, are scaled from those in the lab, r_l. Diapir volumes range from 45 to 700 km^3. †Thermal diffusion time, t_d, is calculated by $t_d = r_m^2/\kappa$, where κ is the thermal diffusivity of the mantle ($\kappa = 10^{-2}$ cm^2 s^{-1}). ‡Ascent times in the mantle, t_m, are scaled from laboratory ascent times, t_l. The velocity ratio U^* from Eq. 1 introduces a time scale, allowing us to relate laboratory times to the mantle through the relation $t^* = U_0 t/D$, where t^* is a dimensionless time. §A value for $\Omega \ll 1$ (Fig. 3, path b) is calculated assuming a percolation velocity of 14 cm year^{-1} (*6*), a grain size length scale, and an ascent path length of 100 km. ‖Recent studies have shown water to reduce the viscosity of olivine by between two and three orders of magnitude (*28*). Melt retention may further reduce the viscosity of ascending buoyant material (*29*). ¶The upper extreme of this range of volume fluxes corresponds to diapir production from a ~200-m-thick by 70-km-wide (i.e., along strike) hydrous layer directly above a 10 cm year^{-1} subducting slab, comparable to the results of Marsh (*1*).

conduit networks fulfills a number of observational constraints including the rapid transport times required by recent U-Th disequilibrium (*11–13*) and ^{10}Be (*9*) studies, the observed episodicity of volcanic production at arcs (*1*), and ascent trajectories in *P-T* space that allow hydrous material to enter the subarc region within the melting field, avoiding substantial freezing out of melt during ascent. Rapid vertical transport along conduit networks may also explain the sustained, high-volume magmatism observed at some arcs (*23*).

References and Notes

1. B. D. Marsh, *J. Geol.* **87**, 687 (1979).
2. Y. Tamura, *J. Petrol.* **35**, 619 (1994).
3. M. Sakuyama, *J. Volcanol. Geotherm. Res.* **18**, 297 (1983).
4. Y. Tatsumi, M. Sakuyama, H. Fukuyama, I. Kushiro, *J. Geophys. Res.* **88**, 5815 (1983).
5. M. Nakada, Y. Takeda, *Tectonophysics* **246**, 147 (1995).
6. M. Spiegelman, D. McKenzie, *Earth Planet. Sci. Lett.* **83**, 137 (1987).
7. J. H. Davies, D. J. Stevenson, *J. Geophys. Res.* **97**, 2037 (1992).
8. Y. Furukawa, *J. Geophys. Res.* **98**, 8309 (1993).
9. J. D. Morris, W. P. Leeman, F. Tera, *Nature* **344**, 31 (1990).
10. M. T. McCulloch, J. A. Gamble, *Earth Planet. Sci. Lett.* **102**, 358 (1991).
11. C. J. Hawkesworth, S. P. Turner, F. McDermott, D. W. Peate, P. van Calsteren, *Science* **276**, 551 (1997).
12. S. Turner, C. Hawkesworth, *Nature* **389**, 568 (1997).
13. T. Elliott, T. Plank, A. Zindler, W. White, B. Bourdon, *J. Geophys. Res.* **102**, 14991 (1997).
14. P. R. Vogt, *Earth Planet. Sci. Lett.* **21**, 235 (1974).
15. R. D. Jarrard, *Rev. Geophys.* **24**, 217 (1986).
16. B. D. Marsh, I. S. E. Carmichael, *J. Geophys. Res.* **79**, 1196 (1974).
17. B. D. Marsh, *Am. Sci.* **67**, 161 (1979).
18. _____, in *The Geophysics of the Pacific Ocean Basin and Its Margins*, G. H. Sutton, M. H. Manghnani, R. Moberly, Eds. (American Geophysical Union, Washington, DC, 1976), vol. 19, pp. 337–350.
19. M. A. Feighner, L. H. Kellogg, B. J. Travis, *Geophys. Res. Lett.* **22**, 715 (1995).
20. P. Olson, H. Singer, *J. Fluid Mech.* **158**, 511 (1985).
21. J. A. Whitehead, K. R. Helfrich, in *Magma Transport and Storage*, M. P. Ryan, Ed. (Wiley, Chichester, UK, 1990), pp. 53–76.
22. B. D. Marsh, *Am. J. Sci.* **282**, 808 (1982).
23. J. Johnson, J. M. Lees, E. Gordeev, *Geophys. Res. Lett.* **25**, 3999 (1998).
24. D. H. Green, *Earth Planet. Sci. Lett.* **19**, 37 (1973).
25. A. B. Thompson, *Nature* **358**, 295 (1992).
26. D. McKenzie, M. J. Bickle, *J. Petrol.* **29**, 625 (1988).
27. C. Kincaid, I. S. Sacks, *J. Geophys. Res.* **102**, 12295 (1997).
28. G. Hirth, D. L. Kohlstedt, *Earth Planet. Sci. Lett.* **144**, 93 (1996).
29. _____, *J. Geophys. Res.* **100**, 15441 (1995).

30. This paper benefited from the input of the many participants at the August 2000 MARGINS Theoretical Institute in Eugene, OR, and two anonymous reviewers. This work was supported by NSF grants EAR-92-19796 and EAR-96-28739.

7 March 2001; accepted 25 May 2001

Evidence for a Large-Scale Remnant of Subducted Lithosphere Beneath Fiji

Wang-Ping Chen[1,2]* and Michael R. Brudzinski[1]

We combine spatial variations of *P*- and *S*-wave speeds, 1000 fault plane solutions, and 6600 well-determined hypocenters to investigate the nature of subducted lithosphere and deep earthquakes beneath the Tonga back-arc. We show that perplexing patterns in seismicity and fault plane solutions can be accounted for by the juxtaposition of a steep-dipping Wadati-Benioff zone and a subhorizontal remnant of slab that is no longer attached to the actively subducting lithosphere. The detached slab may be from a previous episode of subduction along the fossil Vitiaz trench about 5 to 8 million years ago. The juxtaposition of slabs retains a large amount of subducted material in the transition zone of the mantle. Such a configuration, if common in the past, would allow the preservation of a primordial component in the lower mantle.

The interaction between subducted lithosphere and the transition zone of the mantle is a key issue in geodynamics. In particular, the amount of slab penetration into the lower mantle controls the rate of heat and mass transfer between the upper and the lower mantle (*1–3*). The Tonga subduction zone is a natural laboratory for studying this issue because large amounts of old, cold slab have been rapidly subducting in the past 50 to 100 million years *(4–6)*. Presently, the rate of subduction exceeds 200 ± 40 mm/year *(7)*.

Considering the old age of the Pacific lithosphere being subducted and the extremely fast rate of convergence, subducted material beneath Tonga should have caused the most prominent thermal anomaly in the mantle (*8*, *9*). However, global travel-time tomography showed only moderate anomalies of fast *P*- and *S*-wave speeds (V_P and V_S) in the lower mantle along the Tonga subduction zone (*10*, *11*), implying that a large amount of subducted material remains in the upper mantle. If so, how are large-scale remnants of slab accommodated in the transition zone? This issue pertains to the current search for a primordial mantle (*12*, *13*). The more slab material that remains in the transition zone, the easier it is to preserve a primordial component in the lower mantle.

It is a basic tenet of plate tectonics that earthquakes deeper than about 100 km occur in the cold interior of subducted lithosphere (*14–16*). Otherwise, deep earthquakes would not be restricted to zones of recent convergence. Many researchers have noted the complexity of seismicity in the Tonga-Fiji region (*17*, *18*). A unique feature is a subhorizontal swath of deep (>300 km) outboard earthquakes that extends several hundred kilometers farther to the west of the Wadati-Benioff zone (WBZ) (*19*, *20*). The WBZ, which marks the trace of actively subducting lithosphere, is defined by an inclined zone of seismicity connecting shallow earthquakes near the trench with the deepest earthquakes in the mantle (Figs. 1 and 2).

The wide extent of the outboard earthquakes provides a favorable configuration for modeling high-resolution, broadband *P* and *S* waveforms to precisely determine V_P and V_S of the earthquake-generating (seismogenic) material (*21*, *22*). In the transition zone of the mantle, seismic wave speeds are mainly a function of temperature and petrology. In the source region of outboard earthquakes, seismicity independently indicates cold temperature, a condition expected to raise both V_P and V_S. However, a petrologic anomaly to trigger the outboard earthquakes could counteract the thermal effect on wave speeds—a key point to bear in mind.

Here, we first seek to unravel the perplexing pattern of deep seismicity beneath Tonga (Fig. 1). The data include well-determined fault plane solutions of 1000 large- to moderate-sized earthquakes (*17*, *20*, *23–27*) and precise locations of 6600 hypocenters (*28*, *29*). The results are then combined with spatial variations of V_P and V_S to show that a remnant slab lies subhorizontally above the active, steep-dipping WBZ.

To illustrate the relation between the outboard earthquakes and the WBZ, we examine a sequence of 18 cross sections normal to the trench and parallel to the direction of active convergence. For the cross section A–A′ (Figs. 1 and 2A), a continuous band of seismicity, extending from near the surface to depths close to 700 km, defines a clear WBZ with an average dip of about 60°. In addition, fault plane solutions for events in the WBZ show a uniform pattern of down-dip compression, with the axes of maximum com-

[1]Department of Geology, University of Illinois, Urbana, IL 61801, USA. [2]Mid-America Earthquake (MAE) Center, University of Illinois, Urbana, IL 61801, USA.

*To whom correspondence should be addressed. E-mail: w-chen@uiuc.edu